J Mater Sci (2011) 46:6633–6641
DOI 10.1007/s10853-011-5614-5

# Synchrotron X-ray computed microtomography investigation of a mortar affected by alkali–silica reaction: a quantitative characterization of its microstructural features

**Marco Voltolini · Nicoletta Marinoni · Lucia Mancini**

Received: 13 December 2010 / Accepted: 7 May 2011 / Published online: 19 May 2011


**Abstract** Alkali–silica reaction (ASR) is one of the most important weathering processes in cement-based materials. The damages caused by ASR have been qualitatively investigated with a number of different techniques. In this study, we present a procedure to obtain quantitative morphological parameters of the ASR reaction effects using synchrotron X-ray microtomography data. We found three different kinds of voids due to the effect of three different mechanisms: (i) cracks from ASR expansion, (ii) irregular-shaped voids due to the aggregate particles dissolution, and (iii) bubbles due to the cement paste preparation. We were able to separate them using morphological parameters (such as surface/volume ratio and aspect-ratio) calculated for each object, thus obtaining, e.g., volume fractions for each kind of voids. From the orientation data, we also studied if any shape preferred orientation was present in the sample, concerning the fractures network, and we found no appreciable preferred orientation. The new analysis procedure we applied in this study proved to be an effective approach for the quantitative characterization of the effects (cracks and porosity development by aggregate weathering) of the ASR reaction in mortars.

M. Voltolini · L. Mancini
Sincrotrone Trieste S.C.p.A, S.S. 14, km 163,5 in Area Science Park, Basovizza, 34012 Trieste, Italy

N. Marinoni
Dipartimento di Scienze della Terra "Ardito Desio", Università degli Studi di Milano, Via Botticelli 23, 20133 Milan, Italy

*Present Address:*
M. Voltolini
Dipartimento di Geoscienze, Universita' di Padova, via Giotto 1, 35137 Padova, Italy

M. Voltolini (✉)
European Synchrotron Radiation Facility, ID22, 6 rue Jules Horowitz, BP 220, 38043 Grenoble Cedex, France
e-mail: marco.75v@gmail.com

## Introduction

In the last decade, synchrotron radiation computed microtomography (SR micro-CT) has been fully recognized as an extremely valuable technique for characterizing the microstructure of materials. The high contrast and spatial resolution obtained on the images coupled with the possibility of directly handling three-dimensional data, as well as the non-destructive nature of this kind of analysis, makes SR micro-CT well suited for an extremely broad scientific community. Examples of applications of this technique range from medical sciences (e.g., the characterization of bone tissue scaffolds, as in [1, 2]), to earth sciences (e.g. to describe the texture of volcanic products, as in [3]), paleontology (see, e.g., [4]), food science (e.g., to characterize the voids distribution in bread as in [5, 6]), and materials science (e.g., to describe the structure of metallic foams, as presented by [7]).

As a whole, by X-ray micro-CT data analysis we can extract microstructural information, allowing to better understand the main physical phenomena occurring during the formation or the alteration of materials. In particular, SR micro-CT proved to be a powerful tool for the characterization of cement-based materials: [8] performed an investigation of the cement hydration processes, whereas [9] and [10] investigate the cement porosity and the leaching process affecting cement-based materials, respectively. The same approach can be successfully applied to monitor the effect of weathering processes such as alkali–silica reaction (ASR).

Despite its importance as a weathering process, ASR has not been extensively studied by means of X-ray micro-CT and few examples are found in literature [11, 12]. The ASR weathering of cement-based materials can be described as a chemical reaction between alkalis Na and/or K and $OH^-$ supplied by the cement paste with certain silica phases (i.e., opal, chalcedony, and $\alpha$-$SiO_2$) in some aggregate lithologies [13], producing an amorphous and hydraulic silica gel. This gel expands after reaction with water, inducing cracks and fractures in the surrounding concrete [14]. Deleterious ASR was first recognized by Stanton in 1940 [15]. Since then, ASR damage reaction has been identified in many kinds of structures around the world [16]. The investigation of the concretes affected by ASR by means of SR micro-CT allowed gathering an excellent 3D rendering of the reactive aggregate dissolution as well as of the micro-fracture system growth in the weathered structures, thus supplying a major step in the understanding of the ASR mechanism [11]. SR micro-CT proved to be an ideal tool for cement-based materials affected by ASR also because, in contrast with many other techniques, including scanning electron microscopy (SEM) and mercury intrusion porosimetry, it can directly provide 3D information about the weathered samples in a non-destructive analysis. Hence, when combined with 3D image analysis techniques, quantitative data can be extracted.

With respect to the [11] work, the aim of this study is to go a step further, trying to obtain quantitative morphological parameters of the voids in the sample, so the effect of the weathering could be also quantified. In particular, starting from the qualitative study of the ASR phenomenon presented in the article cited above, we applied state-of-the-art quantitative analysis software tools [17, 18] to extract information about the microstructure evolution, i.e., pores, microcracks, and aggregate dissolution, in mortars affected by ASR. More specifically, we propose a method aiming to relate the morphological parameters of voids with the evolution of the ASR weathering.

## Experimental

### Preparation and sampling

The specimen for the SR micro-CT experiment was prepared by mixing Ordinary Portland Cement (CEM I-42.5) with a known content of water and aggregate, the latter constituted by chert and partly silicified mudstone fragments. The siliceous aggregate is angular in shape, with a low crystallinity and with a few fossils whose hollows are preferentially filled with cryptocrystalline quartz and chalcedony. Mechanical sieving was used to separate the aggregate fraction with a size between 0.5 and 1 mm, in order to have a significant number of aggregate fragments in the sample.

The mortar sample, approximately 50 mm high and 5 mm in diameter, was prepared with an aggregates-to-cement paste ratio of 70:30% by volume and a water-to-binder ratio of 0.5 by weight. Cement and aggregates were mixed by hand for few minutes, then injected with a syringe into a mold. The sample was then cured at 20 °C and 25% R.H. throughout the day, and subsequently at 50% R.H. during the following 27 days. After curing, the sample was removed from the mold and immersed into 1 M NaOH solution at 80 °C. Then, it was picked up after 14 days of aging. The sample for micro-CT was obtained by sawing one end of the mortar bar to obtain a $5 \times 5 \times 20$ mm prism.

### Expansion testing

The aggregate reactivity has been tested according to RILEM AAR-2 [19]. Many of the experimental details have been provided in the reference [19], so that only a brief summary will be presented hereafter. The aggregates used for testing have been crushed down to sand-size (grain size ranging from 125 μm and 4 mm), and graded according to the specified size outlined in RILEM protocol.

Three mortar prisms were prepared by mixing aggregate and cement OPC (CEM I-42.5) with a ratio of 2.25 and by considering a water–cement ratio of 0.47 by mass. Three mortar bars of $25 \times 25 \times 28.5$ mm have been compacted. They were cured for 24 h in an environmental chamber at 95% RH and $20 \pm 2$ °C, then were submerged at 80 °C 1 M sodium hydroxide solution for 14 days. The relative amount of expansion of mortar prism was calculated and expressed in %; the result presented in the "Results" section refers to a mean of expansions of three prisms after 14 days of aging.

### Optical microscopy (OM)

Thin sections of the weathered mortar samples were prepared to verify what actually has been expanding in the mortar prisms aged according to RILEM AAR-2 since throughout literature, it is well-known that "low expansion" is not per se synonymous to "non-reactive". In particular, thin sections were studied with an AusJena Jenapol large petrographic microscope in transmitted plane polarized light and crossed polarized light using $5 \times 10 \times 20 \times 50 \times$ objectives. Micrographs were acquired using a Nikon Coolpix 990 digital camera at $2272 \times 1704$ (=3.8 Megapixel) resolution.

### Scanning electron microscopy

Secondary electron images were performed using a Cambridge Stereoscan 360 SEM with an acceleration current of

15 kV, a beam size of ~100 nm and a working distance of 11 mm. The image resolution is of 1024 × 730 and 1.5 μm corresponds to 1 pixel.

### Synchrotron radiation computed microtomography

The hard X-ray imaging experiments were performed at the SYRMEP beamline of the third generation Synchrotron Light Laboratory (Elettra) located in Trieste (Italy).

At SYRMEP, the X-ray source is a bending magnet and the beamline provides, at a distance of about 23 m from the source, a monochromatic, laminar-section X-ray beam with a maximum area of about 160 × 6 mm at the sample stage. The monochromator is based on a double Si(111) crystal system working in Bragg configuration that can be tuned in an energy range of 8.3–35 keV with an energy resolving power of about $10^{-3}$.

Due to the small angular source size and the simple design of the beamline, the photon spot in the experimental hutch is characterized by a good level of spatial coherence (transversal coherence length of about 10 μm at 15 keV) then allowing to perform phase-contrast imaging by using free space propagation. For this study, the tomographic images were acquired in edge detection mode [11, 20] to take advantage of phase-contrast effects, which enhance the smaller features present in the samples.

For the measurements, samples were mounted onto a high-resolution rotation stage and illuminated with a monochromatic radiation (energy = 25 keV). For each tomographic scan, 1440 projections of the sample were acquired for equally spaced rotation angles and measurement time of about 1 s over a total rotation of 180°. The projections were recorded with a 12 bit water-cooled CCD camera (4008 × 2672) px, (9 × 9) μm pixel size. In this case an active input area of 18 (h) × 12 (v) mm is imaged on the sensor. To optimize the phase-contrast effects, the sample-to-detector distance was set to 200 mm.

In order to reconstruct a 3D image of the sample, the tomographic projections were elaborated using a custom-developed software written in IDL® language and based on the filtered backprojection algorithm [21]. The 2D reconstructed slices were visualized by using the ImageJ freeware software [22] while the 3D renderings were obtained by the commercial software VGStudio MAX® 2.0.

### Digital image processing

The first step for the 3D analysis is the selection of a Volume of Interest (VOI) from the data set. The resulting volume was 450 × 343 × 300 voxels. We chose the largest possible subvolume from the original data set to have the more statistically meaningful data. Due to the large size of the aggregate particles it is difficult to say how large a true representative elementary volume needs to be anyway the data showed an acceptable consistency by checking the porosity variation for each slice. The meaningfulness of the morphological parameters we are more interested in depends mainly on the number of objects (the voids, in the case) and since these objects are small with respect to the VOI size, and their total number is in the order of magnitude of $10^3$, we can assume a satisfactory statistical consistency. Once the subvolume was selected, by using the Pore3D software [18] we applied a 3D bilateral filter [23] to reduce the noise of the data set before choosing a proper value for thresholding, in order to obtain a binary volume where the voids were separated from the solid phases. Once the binary volume has been obtained, the morphological characteristics of the voids were determined using the Blob3D software [17]. In Blob3D, voids can be separated manually by a procedure based upon 3D eroding and dilating cycles. In the sample, very little intervention was needed because of the already good separation of the voids. For each object, its volume, surface, aspect-ratio, and orientation were measured. Volumes and surfaces were then used to calculate the sphere-normalized surface/volume ratio that gives a better idea of the surface complexity of the object than the simple surface-to-volume ratio. With this parameter a sphere, of whatever size, would have a value equal to 1, then the more irregular the object, the higher this parameter would be. So the surface/volume ratios cited in this work have all been normalized with respect to a sphere of the same volume, for each object. Voids cut by the subvolume surfaces were not considered for the morphological parameters extraction, but of course were considered when calculating the total volume of the voids to provide the total porosity of the sample. The choice of those morphological parameters was planned to separate the three kinds of voids present in the sample: the original voids of the cement paste (mostly spherical bubbles), the voids due to the dissolution of the aggregate particles (very irregular in shape, with a large surface/volume ratio), and the fractures (characterized mainly by their large aspect-ratio). We also decided not to consider objects smaller than 70 voxels for the calculation of the morphological parameters, since objects described by a small number of voxels would lead to artifacts, so a total of 3198 objects were used in the analysis. Objects described by a low number of voxels are also likely dramatically modified in shape by filters such as the ones used for smoothing, we decided to keep filtering to a minimum, using only a simple 3D bilateral filter, but we decided nevertheless not to consider the smallest objects. Shape Preferred Orientation (SPO) parameters (orientation of the axes of the ellipsoid fitting each object) were calculated to check if any preferred orientation of cracks was present in the sample. Preferred orientation of cracks was studied

selecting the 500 voids with the higher aspect-ratio values and calculating an orientation distribution function (ODF) with a series of custom-made Matlab® scripts [24] based on the MTEX library [25]. Once the ODF is obtained, pole figures (PFs) of the maximum and minimum elongation axes of the objects can be plotted.

## Results

It is widely accepted that ASR can cause serious expansion and cracking in cement-based materials with the formation of the "soft and fluid hydrated alkali silicate" gel [26]. This gel increases in volume when in contact with water and exerts an expansive pressure inside the materials, causing spalling and loss of strength of the concrete.

The ultra-accelerated mortar bar tests according to RILEM AAR-2 [19] show 14-day expansion of the sample exceeding the predefined 0.1% *l*/*l* limit, with an average value (since 3 mortar bars were used) of 0.45% *l*/*l*. In particular, an average length change of the three mortar bars exceeding the predefined <0.1% *l*/*l* limit after 14 days testing is generally accepted as expansive.

Cement-based materials affected by ASR are usually characterized by means of light or electron microscopy, relying on the presence of a reaction rim at the cement and aggregate boundary as well as on a widespread micro-cracking, which develops in the aggregates and then propagates in the cement paste. In the studied mortars, typical features associated with ASR are observed, such as dark rim around siliceous aggregate, cracks filled with gel extending into the cement paste and connecting aggregates particles, cracks passing through aggregates and through cement paste (Fig. 1). Hence the SEM images observations, coupled with qualitative local EDS chemical analyses, pointed out the presence of a Na-rich ASR gel surrounding siliceous aggregates.

As a whole, the feedback that it is possible to obtain from conventional imaging techniques, such as OM and SEM, highlights some disadvantages: all these techniques require a sample preparation that may lead to artifacts. For instance, during the thin section preparation, the polishing might produce artificial cracking and an additional porosity within the ASR-weathered samples. In addition, OM and SEM investigations exhibit severe limits due to the lack of information in the third dimension. These main drawbacks can be overcome by performing micro-CT experiments, which provide a 3D visualization of the investigated samples. In particular the micro-CT combined with the 3D image analysis allows extracting directly volume information within the samples: for instance, it is now possible to extract the real size as well as the spatial distribution and their connectivity of air voids and microcracks within the ASR-weathered materials.

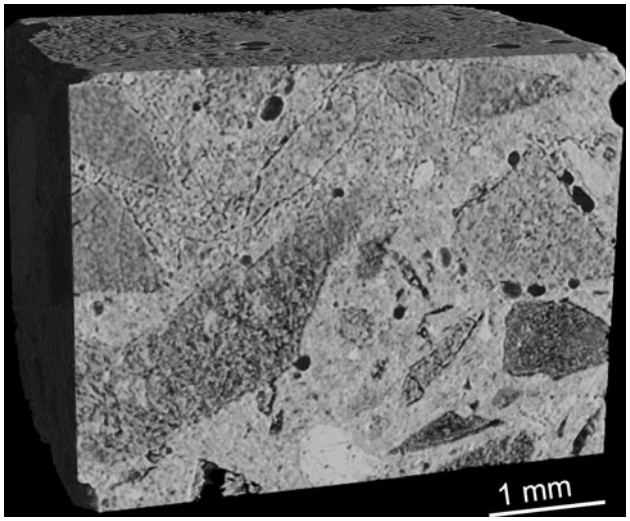


**Fig. 2** Volume rendering of the VOI used for the analysis

### XR micro-CT data analysis

The volume rendering of the VOI selected from the weathered sample used in our analysis is reported in Fig. 2, emphasizing that the ASR promotes the siliceous

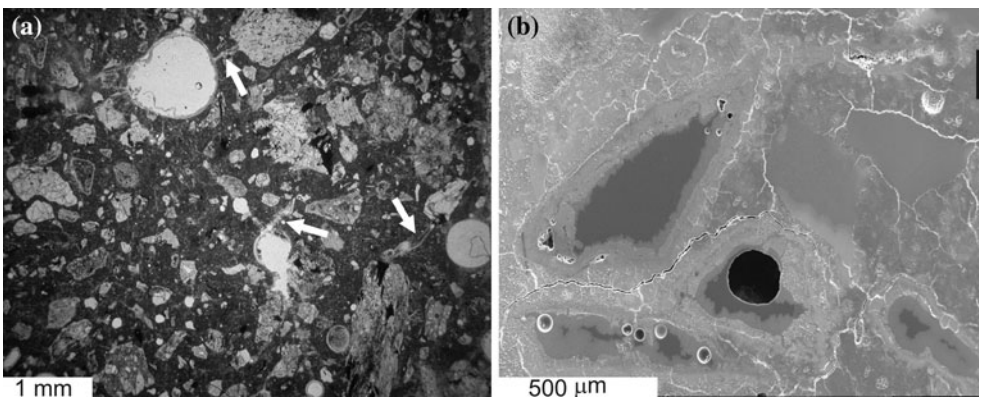


**Fig. 1** Micrographs showing cracks within the cement paste and aggregate dissolution in the ASR-weathered mortar: **a** optical micrograph (crossed polars), with some of the larger cracks highlighted by an *arrow* and **b** backscattered electron image

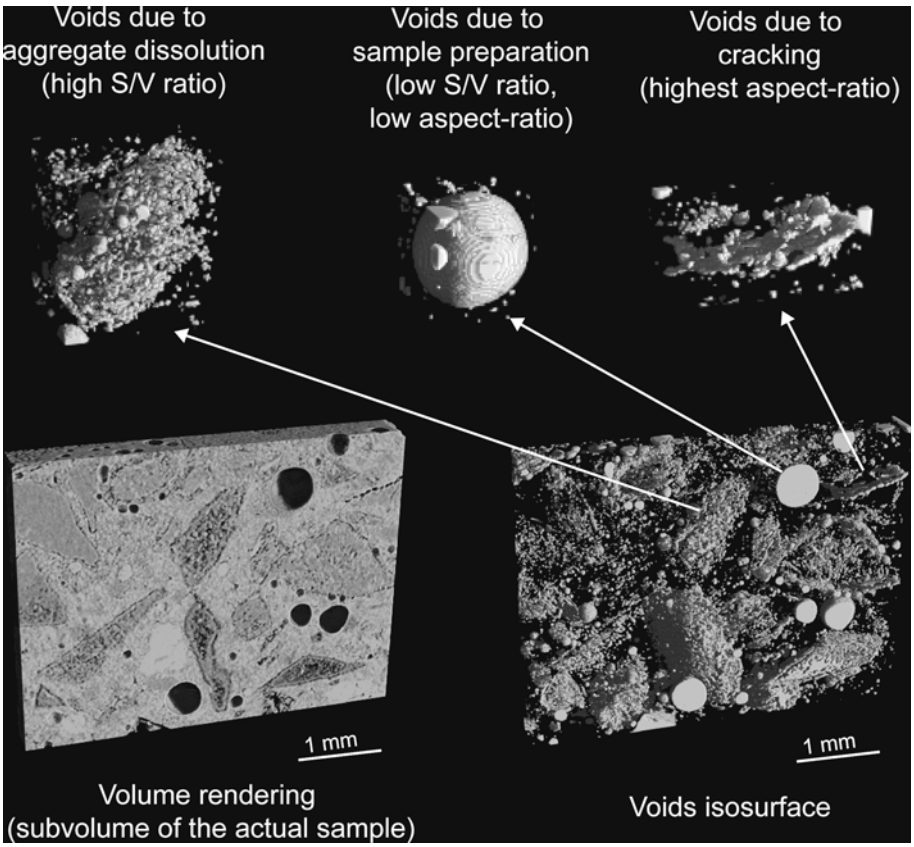


**Fig. 3** Volume rendering of subvolumes to highlight the morphological features of the different kinds of voids in the sample: bubbles due to sample preparation, cracks due to ASR expansion mechanisms, voids due to aggregate dissolution and gel drying. A thin slice from the VOI is provided to highlight the three typical voids features within the sample

ASR-reactive aggregate dissolution: in particular the dissolution starts at the boundary cement paste-aggregate as well as on the aggregate surface, giving a total porosity of 12.0%. Hence, microcracks are clearly visible within the cement paste as well as at the boundary aggregate-cement paste. The cracks, micrometric in size, seem to be isolated within the cement paste as well, as they appear interconnected each other within the cement paste or connected with air voids.

A closer examination of the 3D reconstructed volumes allows the extraction of some quantitative parameters for defining the weathering products (i.e., microcracks and other air voids) within the ASR affected samples. A simple segmentation based on the gray level value (i.e., "thresholding") isolates voids partly due to sample preparation and aggregate dissolution and partly due to the microcracks growth within the weathered samples. These voids can be easily differentiated by their morphological features (Fig. 3): the voids occurring during the sample preparation are mostly spherical bubbles of air entrapped during the mixing of the cement powder with the water; they are usually quite large spherical bubbles, showing a small surface/volume ratio (normalized to a sphere) and a small aspect-ratio as well. The second group includes the voids that are created because of the aggregate dissolution: the alkaline solution dissolves the reactive particles, the ASR gel fills, totally or in part, the voids created by the process and then dries, resulting in groups of spongy-like voids characterized mainly by their high surface/volume ratio. The aspect-ratio of these voids due to the dissolution process is usually small. Finally, the third group comprises cracks due to the expansion of the ASR gel: their surface/volume ratio is expected to be medium to medium–high and their aspect-ratio values are high by the definition of the term "crack" itself. Cracks are often partially filled with the ASR gel, and their size is often not very large, making them sometimes difficult so identify. Therefore, by considering these morphological features, we can identify and separate three kinds of voids occurring in the ASR-weathered samples.

If we consider the volumes of the single objects extracted after the segmentation process in the weathered samples, a volume frequency histogram can be calculated as reported in Fig. 4a. This graph shows that there are a large number of small objects associated with few bigger ones (mainly the original bubbles of the cement paste plus some of the most weathered and largest aggregate particles). More interesting is the histogram in Fig. 4b where the voids surface/volume ratio (again, normalized to a sphere) versus frequency is plotted. It is possible to see that, at values close to 1, the objects are almost spherical in shape, and are likely the bubbles created during the sample

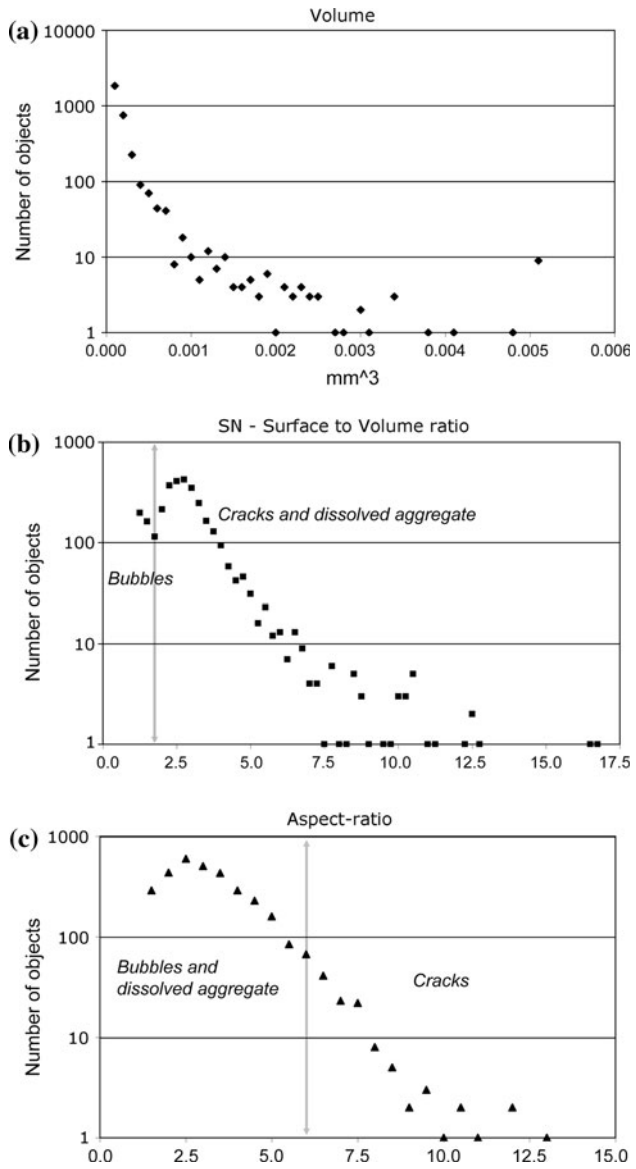


**Fig. 4** Plots showing the results of the morphological study of 3198 voids. In **a**, the volume frequency plot is shown; **b** the sphere-normalized surface/volume ratio frequencies are plotted; **c** the aspect-ratio frequencies are shown. *Gray arrows* show the limits set for the different kinds of void separation. All plots are shown with the "number of objects" axis in log scale

preparation. Moving to higher values, we get the voids due to the cracking and the aggregate dissolution processes; indeed, a significant number of objects with the highest surface/volume ratios are clearly recognized and can be ascribed to the dissolution of the aggregate particles, leading to the largest spongy-like voids. Many of the voids crated by the aggregate dissolution are in any case separated by the dried gel and form groups where the surface/volume ratio is smaller and likely to overlap with the ones due to the cracks. These smaller voids frequently appear in the weathered mortar, thus contributing to the total porosity of the sample.

To sort out cracks form the voids due to both dissolution and sample preparation, the frequency histogram of the aspect-ratio values for the voids is plotted (Fig. 4c). It is quite clear that the majority of the voids show low values (bubbles and dissolution voids are the majority), but there is a remarkable amount of objects with high aspect-ratio, and we found the value of 6 the most proper to separate cracks from other voids.

To summarize, by analyzing these plots we are able to identify and quantify three different kinds of voids in the weathered mortars according to their morphological features in a quite straightforward way. For this purpose, we need to set arbitrary parameters (i.e., the aspect-ratio value) to separate these three kinds of voids. The choice of these parameters is of paramount importance and needs to be expressed in the results for several reasons: (i) to the knowledge, no fixed rule for setting the values of the above cited parameters exists in literature. For instance, the aspect-ratio value for separating cracks and voids is usually set arbitrarily by the authors; (ii) the same value of the parameters should be adopted when a comparison among different samples is performed. In so doing, from a total number of 3198 objects we decided to set a limit in the aspect-ratio of the objects to separate cracks from other voids. In particular, we found that 6 is a reasonable limit and so we felt that the 111 objects with aspect-ratio $\geq 6$ can be safely considered cracks. To separate the remnant objects (bubbles and voids attributed to the aggregate dissolution) the best strategy is to set a limit on the surface/volume ratio. Since bubbles in this sample are almost perfect spheres we decided to set a value of 1.75, so all the voids with a shape quite close to a sphere would be considered as bubbles due to the sample preparation. Setting this limit, 476 bubbles (and therefore 2611 voids attributed to the sample dissolution) are found. It is then straightforward to correlate these numbers with the total volumes of the objects to find some more interesting information. As expected, cracks have a very small impact on the sample total porosity: cracks account for the 3.5% of the total number of the objects, and even less, only the 2.9%, of the total porosity. Cracks are very thin, and therefore their contribution to the porosity is almost negligible. The bubbles associated with air entrapped during mortar preparation are 14.9% in number, but correspond to the 21.8% of the total porosity. Again, these values confirm what we were expecting since the air bubbles are usually fairly large (as also seen in the volume rendering figures). Finally, we can see that the voids due to dissolution are 81.3% in number, thus contributing for the 75.6% of the total porosity (reminding that for this sample we found a total

**Table 1** Fractions of the three kinds of voids in the weathered sample, obtained by considering their morphological features (sample total porosity is 12.0%)

| | Volume ($mm^3$) | Number of objects | Number of objects (%) | Volume (%) |
|---|---|---|---|---|
| Cracks | 0.020 | 111 | 2.9 | 3.5 |
| Bubbles | 0.151 | 476 | 21.8 | 14.9 |
| Dissolved aggregate | 0.521 | 2611 | 75.3 | 81.6 |
| Total | 0.692 | 3198 | 100 | 100 |

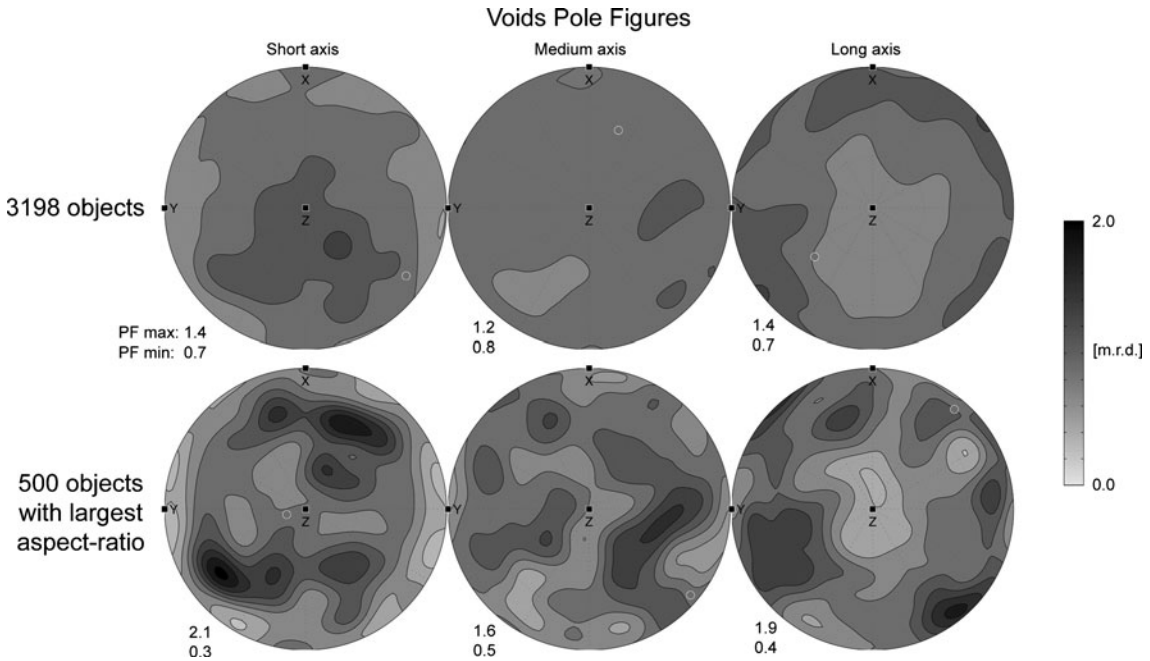


**Fig. 5** Pole figures obtained from ODFs calculated from the orientation parameters of the ellipsoids used to fit each object. PFs for all the voids considered and for the 500 objects with larger aspect-ratio are shown. Intensity values are in multiples of random distribution (m.r.d.). *Circles* represent the mean orientation. Equal area projection

porosity of 12.0%). These results are summarized in Table 1.

The results on the frequency histogram confirm the preliminary observations edited in the past study [11]: the ASR-weathered sample is characterized by voids due to dissolution rather than microcracks, thus suggesting that the ASR, in these experimental conditions, promote the aggregate dissolution in spite of microcracks. This is somehow in contrast with the observations performed by means of OM and SEM. In particular, the investigations on different weathered samples by means of the conventional imaging techniques pointed out an increase in the microcracking as the weathering time proceeds whereas this is not the case for the 3D experiments where a clear decrease of the number of microcracks is observed, thus suggesting that the coalescence mechanism is predominant. The main reason for this difference is that microcracks may seem disconnected in 2D while they are connected in 3D [8].

Another microstructural feature we decided to check is if voids and cracks, in particular, show any SPO. Once obtained the direction cosine matrix (DCM) of each object it is possible to calculate an ODF. This function can be calculated choosing the object classes we are interested in. For example, the PFs plotted in Fig. 5 represent the texture by number (TbN), where each object has the same weight, independently by its volume (see, e.g., [27]). It is clear that no evident preferred orientation is present, as expected in a material subject to no restraint (free expansion). The three PFs plotted in figure represent the three axes of the ellipsoid fitting the object (short, medium, and long axes, respectively, in figure). To further confirm that the preferred orientation is almost absent, we get a "texture factor" $F_2$ value $= 1.06$. This value ranges from 1 for perfectly random distribution to $+\infty$ for a single crystal-like distribution (again, see [27]). Since the PFs plotted in Fig. 5 (top) represent the 3198 largest objects, to check cracks preferred orientation we decided to calculate an ODF and the PFs from the objects with the characteristics typical of the cracks: so we chose the 500 objects with the higher aspect-ratio. The PFs obtained are plotted in Fig. 5 (bottom). It is possible to see that PFs maxima are higher than the previous PFs; also the texture factor $F_2$ is a little higher, reaching a value of 1.32. This could suggest that some preferred orientation is present, even though it is very

weak. This is only partially true since the ODF calculated with a lower number of objects can provide a "sharper" texture because of the poorer statistics of the objects distributed in the ODF cells. This is likely the reason of the higher values obtained. This effect also affects PFs minima, giving too low values, while maxima values are much less affected by this problem. Nevertheless from the PFs it is possible to see that two weak maxima are evident in the PF relative to the short axes of the ellipsoids fitting the objects. For cracks, this is the most important direction since it is the one perpendicular to the crack surface. From these assumptions, we can see that two weakly oriented systems of fractures are present, but it seems to be due chiefly to the cracks systems surrounding the bigger aggregate particles. These particles are so large if compared with the investigated volume that can simulate a sort of preferred orientation. Considering all these aspects, it would be safe to state that our sample voids do not show any appreciable preferred orientation, considering either all the groups of voids or the cracks alone.

As a whole, this method proved to work well and it could be successfully applied, even if some drawbacks should be considered. First of all, a representative volume of the studied sample should be considered for extracting microstructural features with statistical significance. Ideally the objects of interest should be described by an adequate number of voxels (thus requiring the higher resolution possible), but also a significant number of objects must be present (thus increasing the actual size of field-of-view needs). Being the field-of-view and resolution inversely related, the user is forced to choose the best compromise for the specific analysis. In our case very small features ($\leq$70 voxels, equivalent to $\sim 5 \times 10^{-5}$ mm$^3$) had to be neglected, thus loosing the smaller features. A measurement with a resolution good enough to consider those features would have forced us to have a VOI with only a couple of aggregate particles, thus leading toward very unrealistic values, e.g., of the porosity. For this reason, we have found that the resolution we are using is an adequate compromise to obtain results that are reasonably significant also for the whole mortar sample. Indeed, the quantitative parameters of SPO can also suffer of poor statistics since a few thousand objects are usually required to get completely reliable results; with fewer objects the minima of the PFs and the texture factor $F_2$ become less reliable. PFs maxima are still significant and the patterns of the PFs can highlight any preferred orientation (or the lack of) nevertheless. Finally, another important issue to consider for this kind of study is the choice of the values to set as limits of the morphological parameters, for the separation of the three kinds of voids. We have set limits that seemed the most proper, considering the frequency distribution plots. This choice will significantly affect the results and no fixed rule is available, so the analyst must give the value of the limits he used in order to make significant comparisons possible.

## Conclusion

In this study, a method for the extraction of quantitative parameters in ASR-weathered mortars, investigated by means of SR micro-CT data, is presented. In particular, three different kinds of voids (bubbles due to the sample preparation, irregular-shaped voids attributed to aggregate dissolution, and cracks from ASR expansion) have been identified and separated by a characterization of their morphological parameters such as surface/volume ratio normalized to a sphere and aspect-ratio. The separation of the different kinds of voids allows obtaining important parameters for the weathering effects characterization, such as their volume fractions. Moreover, we were also able to study the SPO of the objects classified as "cracks" and found no evident preferred orientation.

As a whole, the results highlighted a promising new procedure, to apply on micro-CT data, for obtaining a quantitative characterization of the microstructural features in ASR-weathered mortar samples.

To the knowledge, the quantification of the ASR weathering effects by X-ray micro-CT in mortars has never been done before; therefore, we feel the procedure proposed in this study could be a useful tool for the scientific community involved in the research dealing with the weathering of cement-based materials.

**Acknowledgements** The authors acknowledge an anonymous reviewer for his comments that helped to improve this manuscript and Prof. P.J. Monteiro for helpful discussion during the preliminary stage of this study.

## References

1. Komlev VS, Mastrogiacomo M, Peyrin F, Cancedda R, Rustichelli F (2009) Tissue Eng C 15:425
2. Yue S, Lee PD, Poologasundarampillai G, Yao Z, Rockett P, Devlin AH, Mitchell CA, Konerding MA, Jones JR (2010) J Mat Sci Mater Med 21(3):847
3. Polacci M, Mancini L, Baker DR (2010) J Synchrotron Radiat 17:215
4. Tafforeau P, Boistel R, Boller E, Bravin A, Brunet M, Chaimanee Y, Cloetens P, Feist M, Hoszowska J, Jaeger JJ (2006) Appl Phys A 83(2):195
5. Falcone PM, Baiano A, Zanini F, Mancini L, Tromba G, Dreossi D, Montanari F, Scuor N, Del Nobile MA (2005) Food Sci 70(4):E265
6. Lassoued N, Babin P, Della Valle G, Devaux M-F, Réguerre A-L (2007) Food Res Int 40(8):1087
7. Zhang Q, Toda H, Kobayashi M, Suzuki Y, Uesugi K (2010) Mat Sci Forum 654–656:2358
8. Gallucci E, Scrivener K, Groso A, Stampanoni M, Margaritondo G ((2007)) Cem Concr Res 37(3):360

9. Promentilla MAB, Sugiyama T, Hitomi T, Takeda N (2008) J Adv Concr Technol 6(2):273
10. Burlion N, Bernard D, Chen D (2006) Cem Concr Res 36(2):346
11. Marinoni N, Voltolini M, Mancini L, Vignola P, Pagani A, Pavese A (2009) J Mater Sci 44(21):5815. doi:10.1007/s10853-009-3817-9
12. Monteiro PJM, Kirchheim AP, Chae S, Fischer P, MacDowell AA, Schaible E, Wenk H-R (2009) Cem Concr Compos 31(8): 577
13. Wigum BJ (2006) In: Proceedings of 8th CANMET/ACI International Conference on Recent Advances in Concrete Technology, Montreal, pp 111–128
14. Swamy RN (1992) The alkali-silica reaction in concrete. Blackie, Glasgow
15. Stanton TE (1940) ASCE 66:1781
16. Diamond S (1992) Strategic Highway Research Program Report (SHRP-C/UWP-92-601), p 470
17. Ketcham RA (2005) Geosphere 1:32
18. Brun F, Mancini L, Kasae P, Favretto S, Dreossi D, Tromba G (2010) Nucl Instrum Method A 615(3):326
19. Sims I, Nixon PE (2000) Mater Struct 33:283
20. Cloetens P, Barrett R, Baruchel J, Guigay J-P, Schlenker M (1996) J Phys D 29:133
21. Herman GT (1980) Image reconstruction from projections. Elsevier, New York
22. Abramoff MD, Magelhaes PJ, Ram SJ (2004) Biophoton Int 11:36
23. Tomasi C, Manduchi R (1998) In: Sixth International Conference on Computer Vision, New Delhi, pp 839–846
24. Voltolini M, Zandomeneghi D, Mancini L, Polacci M (2011) J Volcanol Geotherm Res 202(1–2):83
25. Hielscher R, Schaeben H (2008) J Appl Cryst 41(6):1024
26. Ichikawa T, Miura M (2007) Cem Concr Res 37(9):1291
27. Randle V, Engler O (2000) Introduction to texture analysis. Gordon and Breach, Amsterdam